The Astronomical Journal, 156:270 (11pp), 2018 December https://doi.org/10.3847/1538-3881/aae92a

The Albedos, Sizes, Colors, and Satellites of Dwarf Planets Compared with Newly Measured Dwarf Planet 2013 FY27

Scott S. Sheppard[1], Yanga R. Fernandez[2], and Arielle Moullet[3]
[1] Department of Terrestrial Magnetism, Carnegie Institution for Science, 5241 Broad Branch Rd. NW, Washington, DC 20015, USA; ssheppard@carnegiescience.edu
[2] Dept. of Physics, Univ. of Central Florida, Orlando, FL 32816, USA
[3] Universities Space Research Association, SOFIA Science Center, Moffett Field, CA 94035 USA
Received 2018 August 6; revised 2018 October 12; accepted 2018 October 15; published 2018 November 16

Abstract

2013 FY27 is the ninth intrinsically brightest Trans-Neptunian Object (TNO). We used ALMA at thermal wavelengths and *Magellan* in the optical to determine 2013 FY27's size and albedo for the first time and compare it to other dwarf planets. We found 2013 FY27 has a geometric albedo of $p_V = 0.17^{+0.045}_{-0.030}$ and effective diameter of $D = 765^{+80}_{-85}$ km. This puts 2013 FY27 in the transition region between the largest TNOs that have higher albedos and densities than smaller TNOs. No short-term light curve was found, with variations $<0.06 \pm 0.02$ mag over hours and days. The Sloan colors of 2013 FY27 are $g-r = 0.76 \pm 0.02$ and $r-i = 0.31 \pm 0.03$ mag, giving a moderately red color. This is different than the neutral or ultra-red colors found for the 10 largest TNOs, making 2013 FY27 one of the largest moderately red TNOs, which are only seen, and in abundance, at diameters less than 800 km. This suggests something different might be associated with TNOs larger than 800 km. Moderately red colors might indicate old or ice-poor surfaces with TNOs larger than 800 km having fresher or more volatile-rich surfaces. TNOs larger than 800 km could be more differentiated, giving them different surface compositions. A satellite at $0\farcs17$ and 3.0 ± 0.2 mag fainter than 2013 FY27 was found through *Hubble Space Telescope* observations. Almost all the largest TNOs have satellites, which now includes 2013 FY27. Assuming a similar albedo, the satellite is ~186 km in diameter, making the primary $D = 742^{+78}_{-83}$ km.

Key words: comets: general – Kuiper Belt: general – minor planets, asteroids: general – Oort Cloud – planets and satellites: individual (2013 FY27)

1. Introduction

2013 FY27 was discovered on UT 2013 March 17 as part of an ongoing deep and wide survey for extreme Trans-Neptunian objects (TNOs) by Sheppard & Trujillo (2016). The orbit of 2013 FY27, with a semimajor axis near 59 au, eccentricity of 0.39 and inclination of 33 degs, makes it a typical scattered disk object. With a perihelion that comes inside of 36 au, 2013 FY27 can come relatively close to Neptune and have significant gravitational interactions with the planet. The high eccentricity of 2013 FY27's orbit means it experiences large surface temperature variations of some 16 to 22 Kelvin between aphelion and perihelion.

Currently, 2013 FY27 is the ninth intrinsically brightest TNO and one of the most distant at around 80 au, which is near its aphelion. 2013 FY27 is the intrinsically brightest known TNO that has not had its thermal emission measured (Figure 1). The other intrinsically brightest 15 or so TNOs have been observed for their thermal emission by either *Spitzer*, *Herschel*, or ALMA (Stansberry et al. 2008; Brown et al. 2010; Lellouch et al. 2010, 2013, 2017; Lim et al. 2010; Muller et al. 2010; Pal et al. 2012; Santos-Sanz et al. 2012, 2017; Fornasier et al. 2013; Gerdes et al. 2017; Kovalenko et al. 2017). From thermal observations, one can calculate how much sunlight an object absorbs. Optical observations allow one to calculate how much sunlight an object scatters or reflects. These two measurements can then be used to solved for the two unknowns of the size and albedo of an object, using the radiometric method (Lebofski et al. 1986; Harris 1998; Fernandez et al. 2013). Some of the largest TNOs have also been observed to occult bright stars, giving another technique to determine the size and albedos of these objects (Elliot et al. 2010; Ortiz et al. 2012a; Braga-Ribas et al. 2013; Brown 2013; Alvarez-Candal et al. 2014; Benedetti-Rossi et al. 2016; Dias-Oliveira et al. 2017).

Understanding the size and albedo of 2013 FY27 is important in order to put this intrinsically bright object into context of the other dwarf planets beyond Neptune. The largest TNOs may have formed or evolved in a much different manner than the more moderate and smaller objects. The intrinsic brightness of 2013 FY27 means it is near the interesting transition regime between the largest few TNOs, which have high albedos and high densities, and the more moderate and smaller TNOs, which have moderate and lower albedos and densities (Brown 2013). There also seems to be some correlation between the color of a TNO and its albedo and dynamical classification (Lacerda et al. 2014). Most of the largest TNOs have known satellites, which one can use to find the bulk densities of the objects. The densities of the largest TNOs seem to be much higher (~2–3 g cm^{-3}) than for the smaller TNOs (<1 g cm^{-3}; Brown 2013; Grundy et al. 2015; Barr & Schwamb 2016; Ortiz et al. 2017). This suggests the larger TNOs are made of more rock and less ice and have less porosity than the smaller TNOs. The intermediately sized large TNOs, like 2013 FY27, are thus key to understanding where, how, and why this transition in albedo and density occurs. Through thermal and optical observations, we place 2013 FY27 into the context of the largest TNOs.

2. *Magellan* Optical Observations

We observed 2013 FY27 using the *Magellan* 6.5 m telescope at Las Campanas, in Chile on UT 2016 March 8, 9, and 10 and May 3. The IMACS camera was used, which has a pixel scale of 0.20 arcsec per pixel and field of view of about 0.16 square

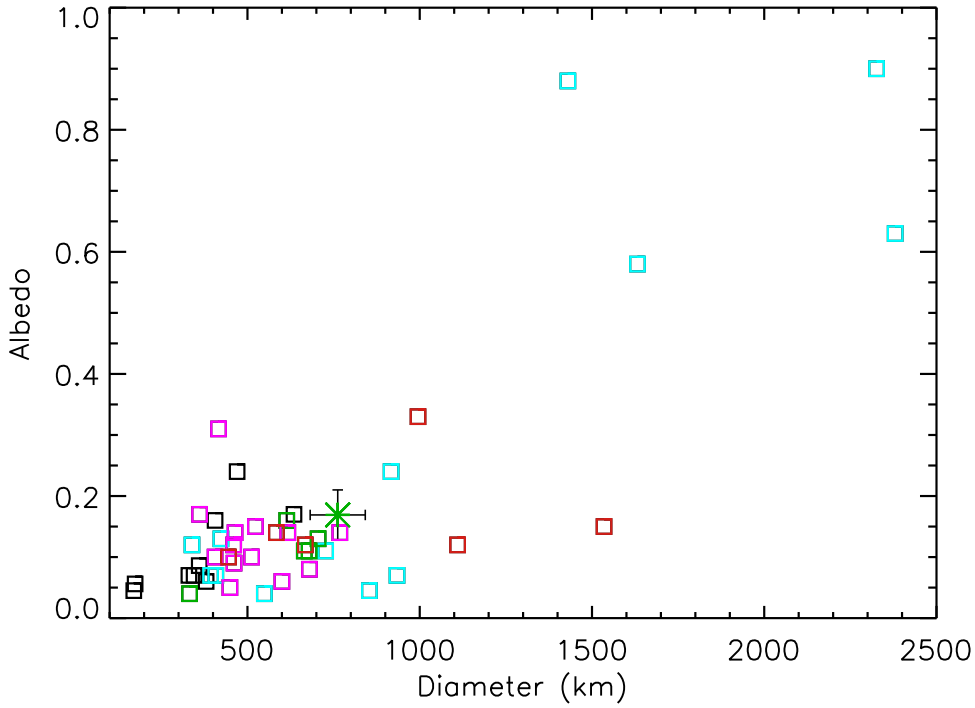

Figure 1. The size vs. albedo of the largest TNOs with well determined characteristics. The largest few TNOs have very high albedos, while the smaller ones are much darker. 2013 FY27 is shown by a green asterisk with error bars. 2013 FY27 is near the large end of objects in the transition region that occurs between the largest and smallest TNOs, making 2013 FY27 important in understanding the transition region. Error bars on other TNOs have been removed for clarity but are generally similar or smaller than 2013 FY27's error bars. The colors of the symbols indicate the visible colors of the objects, with a black symbol signifying no good color measurement. It is apparent that the largest TNOs are bimodal in albedo and color space. The 10 largest TNOs are either neutral to blue in color (blue symbols) with high albedo or ultra-red in color (red symbols) with moderate albedos. There are no very large TNOs with moderately red (green symbols) or very red (magenta symbols) colors. 2013 FY27 is one of the largest moderately red colored TNOs known. The transition from moderately red dominated colors to only neutral and ultra-red colors begins around 800 km in diameter. The albedo dispersion also seems to increase near this size. This might indicate TNOs larger than 800 km have altered their surfaces compared to the smaller objects.

deg. The geometry of the observations are shown in Table 1. All images were bias subtracted and flat fielded with nightly dithered sky twilight flats. Images were obtained guiding at sidereal rates in photometric conditions using the Sloan *g*-, *r*-, or *i*-band filters.

Most of the *Magellan* images were obtained in the *r*-band to look for short-term variability of 2013 FY27 over minutes, hours, and days. To determine the optical color of 2013 FY27, we observed 2013 FY27 multiple times on UT 2016 March 10 in the *g*-band and *i*-band Sloan filters as well as the *r*-band filter. The filters were rotated between the *r*-, *g*-, and *i*-bands to prevent any possible short-term variations from affecting the color measurements and were obtained twice, separated by a few hours. We also convert the Sloan *g, r, i* colors to the Johnson–Morgan–Cousins BVRI filter system for easier comparison to some past works using the transformation equations from Smith et al. (2002): $B = g' + 0.47(g'-r') + 0.17$; $V = g' - 0.55(g'-r') - 0.03$; $V - R = 0.59(g'-r') + 0.11$; $R - I = 1.00(r'-i') + 0.21$. Sheppard (2010) showed these transformations from *g, r, i* colors to BVRI colors are good to within a hundredth of a magnitude for most TNOs.

All the optical observations were calibrated using the Sloan standard star fields DLS1359-11 and PG1633+099. Seeing was between 0.6 and 1.5 arcsec, with longer exposure times used when the seeing was worse. The photometry as well as the details of each individual image from the observations are shown in Table 2. All photometry was obtained similar to that described in Sheppard (2007) and used apertures to fit the variable seeing, ranging from 2.4 in the best seeing to 4 arcsec in the worse seeing. The background counts for each image were subtracted off the photometry of the object using an aperture annulus that was larger than that used for the object's photometry.

Table 1
Geometry of the Observations

Name	UT Date	*R* (au)	Δ (au)	α (deg)	Telescope
2013 FY27	2016 Mar 08	80.26	79.30	0.17	*Magellan*
2013 FY27	2016 Mar 09	80.26	79.30	0.18	*Magellan*
2013 FY27	2016 Mar 10	80.26	79.30	0.18	*Magellan*
2013 FY27	2016 May 03	80.24	79.73	0.62	*Magellan*
2013 FY27	2017 Dec 29	80.09	79.74	0.66	ALMA
2013 FY27	2017 Dec 30	80.09	79.72	0.66	ALMA
2013 FY27	2018 Jan 04	80.09	79.64	0.63	ALMA
2013 FY27	2018 Jan 15	80.08	79.48	0.56	*HST*

Note. Quantities are the heliocentric distance (*R*), geocentric distance (Δ) and phase angle (α). UT Date shows the year, month, and day of the observations.

2.1. r*-band Optical Light Curve*

We observed 2013 FY27 in the *r*-band at *Magellan* over minutes, hours, and days in early 2016 March to look for any short-term variations caused by rotation of the object. The observational results are shown in Table 2. No clear variability was seen, with variability being less than 0.06 ± 0.02 over the three days of observations from 2016

Table 2
Optical Observations 2013 FY27

UT Date[a] yyyy mm dd hh:mm:ss	Airmass	Exp[b] (s)	Mag.[c] (m_r)
2016 Mar 08 01:43:32	1.36	225	21.91
2016 Mar 08 01:48:45	1.34	225	22.00
2016 Mar 08 02:20:38	1.23	225	21.96
2016 Mar 08 02:25:53	1.21	225	21.99
2016 Mar 08 02:56:24	1.15	225	21.95
2016 Mar 08 03:25:11	1.10	300	21.94
2016 Mar 08 04:00:14	1.08	250	21.91
2016 Mar 08 04:46:55	1.08	250	21.89
2016 Mar 08 05:36:42	1.13	300	21.95
2016 Mar 08 07:14:42	1.45	350	21.95
2016 Mar 08 07:35:49	1.58	350	21.95
2016 Mar 09 00:30:34	1.86	400	21.95
2016 Mar 09 00:39:18	1.77	400	21.98
2016 Mar 09 01:15:27	1.49	400	21.99
2016 Mar 09 01:23:45	1.44	380	21.98
2016 Mar 09 01:31:36	1.40	380	21.92
2016 Mar 09 01:54:21	1.30	400	21.92
2016 Mar 09 02:02:28	1.27	400	21.92
2016 Mar 09 02:24:01	1.21	380	21.92
2016 Mar 09 02:31:47	1.19	400	21.96
2016 Mar 09 03:04:00	1.13	400	21.94
2016 Mar 09 03:12:11	1.12	350	21.96
2016 Mar 09 04:11:13	1.07	330	21.92
2016 Mar 09 04:55:11	1.09	350	21.93
2016 Mar 09 05:54:18	1.17	350	21.93
2016 Mar 09 07:21:05	1.51	330	21.94
2016 Mar 09 07:38:33	1.63	280	21.98
2016 Mar 10 01:01:19	1.55	330	21.93
2016 Mar 10 01:31:04	1.38	330	21.93
2016 Mar 10 02:19:26	1.21	300	21.92
2016 Mar 10 02:48:42	1.15	250	21.89
2016 Mar 10 03:31:37	1.09	275	21.92
2016 Mar 10 05:08:40	1.11	220	21.90
2016 Mar 10 06:31:05	1.29	280	21.90
2016 Mar 10 07:38:46	1.67	250	21.94
2016 May 02 23:28:15	1.13	300	22.06
2016 May 02 23:33:56	1.12	250	22.04
2016 May 03 00:47:00	1.08	200	22.03
2016 May 03 02:14:34	1.17	250	22.06

Notes.
[a] Universal date at the start of the integration.
[b] Exposure time for the image.
[c] Apparent red magnitude (r-band), uncertainties are ±0.01 to 0.02.

March 8 to 10 (Figure 2). We also found no short-term variations on 2016 May 3 (Figure 3). To look for any periodicity in the light curve, we used the phase dispersion minimization (PDM) method (Stellingwerf 1978, see also Sheppard et al. 2008) and found no significant periodicity. This suggests 2013 FY27 either has a very low amplitude rotational variability, or that its rotation is longer than a few days time. As 2013 FY27 is a large TNO, it should be mostly spherical in shape due to the strength of its own gravity (Basri & Brown 2006; Rambaux et al. 2017). Any short-term variations would likely be from albedo differences on its surface, which we see no strong evidence for. There is also the less likely possibility that we are observing 2013 FY27 pole-on, and thus would see no rotational short-term variability.

2.2. Sloan Optical Colors

Using the Sloan g-, r-, and i-band observations from *Magellan* described above, we find the colors of 2013 FY27 are $g-r = 0.76 \pm 0.02$ mag and $r-i = 0.31 \pm 0.03$ mag giving $g-i = 1.07 \pm 0.04$ mag (Table 3). Since the majority of TNOs have nearly linear color slopes at visible wavelengths, the basic color of a TNO can be reported as its spectral gradient (see Doressoundiram et al. 2008 and Sheppard 2010). The spectral gradient is the amount of reddening per 100 nanometers and can be found through

$$S(\lambda_2 > \lambda_1) = (F_{2,V} - F_{1,V})/(\lambda_2 - \lambda_1) \quad (1)$$

where λ_1 and λ_2 are the midpoint wavelengths for the filters used and $F_{1,V}$ and $F_{2,V}$ are the flux in the filters normalized to the V-band. We use the g and i filters to determine S for 2013 FY27 as these filters have well separated central wavelengths. For 2013 FY27, we find the optical color spectral slope is $S = 17 \pm 2$. This color is moderately red when compared to other TNO colors taken from Hainaut et al. (2012) and the updated Minor Bodies in the Outer Solar System (MBOSS) data base (Figure 4).

It has been known since the first Kuiper Belt objects were discovered that they exhibit a very wide range of colors with possible color groupings (Luu & Jewitt 1996; Barucci et al. 2005; Perna et al. 2010; Tegler et al. 2016). Ultra-red material is generally considered to have a large red spectral gradient of $S > 25$ (Jewitt 2002; Sheppard 2010, 2012). In Sheppard (2012) there is a noticeable gap in objects from the Cold Classical belt with colors just below $S \sim 20$, so we define $20 < S < 25$ as very red objects. Objects with spectral gradients between about 8 and 20 are considered moderately red while objects with color below this are considered neutral to blue in color.

It is apparent in Figure 4 that the 10 largest TNOs only show extremes in colors, being either very neutral or ultra-red. It is not until objects smaller than about 800 km in diameter start to show very red and moderately red colors. This is interesting as the extreme colors are usually associated with organics and freshly exposed ices such as methane, water ice, nitrogen, and methanol (Barucci et al. 2010; Tegler et al. 2010; Brown et al. 2012; Dalle Ore et al. 2015; Fraser et al. 2015). This suggests the largest TNOs are continuing or have more recently modified their surfaces compared to the TNOs smaller than 800 km. Moderately red colors might be more expected on objects that have old surfaces as micrometeorite bombardment and irradiation would be expected to dull any exposed ices over time (Moroz et al. 2004; Grundy 2009; Lo et al. 2015; Chin et al. 2016; Lantz et al. 2017). The surfaces of the largest TNOs might be fresher because they can more easily hold on to volatile ices and could further have differentiated more completely and even have cryovolcanism occurring in recent times. 2013 FY27 is one of, if not the largest known moderately red object.

2.3. Optical Phase Curve

The optical apparent magnitude of a TNO depends on its radius (r), distance from the Sun (R), distance from Earth (Δ), albedo (p), and phase angle (α). The apparent optical

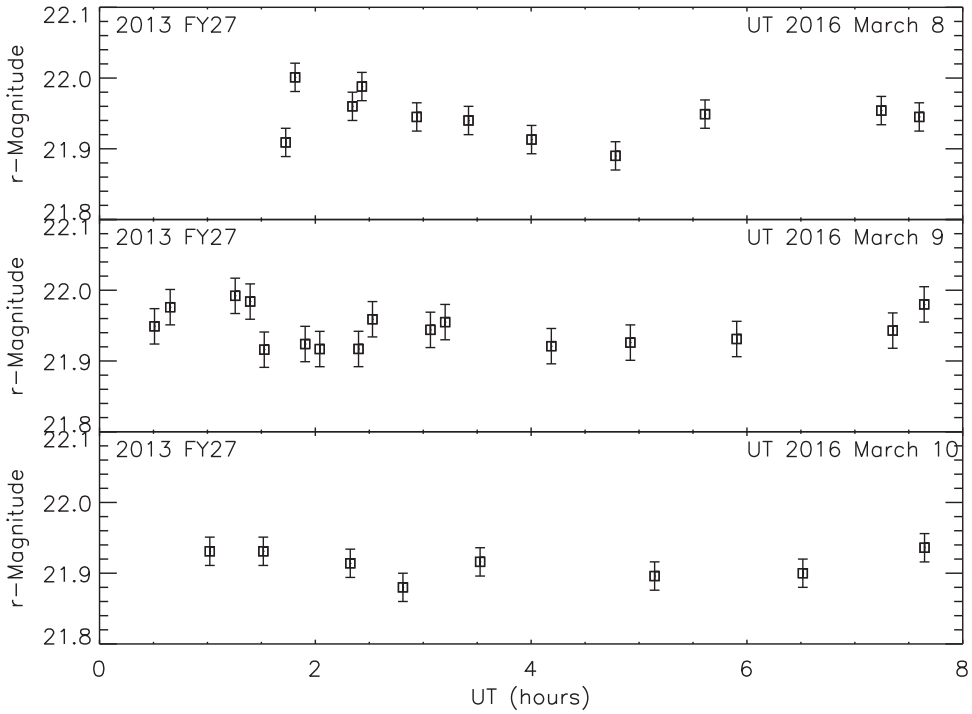

Figure 2. *r*-band photometry over several hours and days for 2013 FY27 from the *Magellan* telescope on UT 2016 March 8, 9, and 10. No obvious rotational light curve is seen over this time, with any variations less than about 0.06 ± 0.02.

Table 3
Properties Found for 2013 FY27

Qtty	Measurement
H	3.15 ± 0.03 mag
$M_r(1, 1, 0)$	2.85 ± 0.02 mag
$M_R(1, 1, 0)$	2.59 ± 0.02 mag
$M_V(1, 1, 0)$	3.15 ± 0.03 mag
$m_r(\alpha = 0.18$ deg)	21.92 ± 0.02 mag
$m_r(\alpha = 0.62$ deg)	22.04 ± 0.02 mag
$g - r$	0.76 ± 0.02 mag
$r - i$	0.31 ± 0.03 mag
$g - i$	1.07 ± 0.04 mag
$m_R(\alpha = 0.62$ deg)	21.79 ± 0.02 mag
$m_V(\alpha = 0.62$ deg)	22.35 ± 0.03 mag
V–R	0.56 ± 0.03 mag
R–I	0.52 ± 0.03 mag
S	17 ± 2
β	0.25 ± 0.03
p_v	$0.17^{+0.045}_{-0.030}$
Effective Diameter	765^{+80}_{-85} km
Primary Diameter	742^{+78}_{-83} km
Satellite Diameter	186^{+25}_{-26} km

Note. H is the absolute magnitude in the *V*-band. The colors are from the Sloan *g*-, *r*-, and *i*-bands and have also been converted to the Johnson–Kron–Cousins system *B*-, *V*-, *R*-, and *I*-bands using Smith et al. (2002). *S* is the spectral gradient of the object as described in Sheppard (2010).

magnitude can be calculated as

$$m_{\rm filter} = m_{\odot} - 2.5 \log [p * r^2 \phi(\alpha) / (2.25 \times 10^{16} R^2 \Delta^2)] \quad (2)$$

where $m_{\odot}$ is the apparent magnitude of the Sun in the filter being used and the linear phase function $\phi(\alpha)$ can be represented as

$$\phi(\alpha) = 10^{-0.4\beta\alpha} \quad (3)$$

where α is the phase angle in degrees and β is the linear phase coefficient in magnitudes per degree. At opposition, $\alpha = 0$ deg, and thus $\phi(0) = 1$.

We further observed 2013 FY27 at *Magellan* on 2016 May 3 over several hours to determine its phase coefficient (Figure 3). Since no significant short-term light curve was found in March, any long-term variations in brightness are likely attributed to the different phase angles observed for 2013 FY27. The 2016 March observations were obtained at a phase angle near 0°.18 while the May observations had the object further from opposition, near 0°.62 (Table 1). Again, 2013 FY27 showed no significant variations over the nearly three hours of observations on 2016 May 3. The average *r*-band magnitude in March was 21.92 ± 0.02 mag and in May 22.04 ± 0.02 mag. 2013 FY27 should have been about 0.01 mag fainter in May because it was slightly further from the Earth at that time. Thus, 2013 FY27 was about 0.11 mag fainter in May when accounting for differences in its distance from the Sun and Earth. We attribute the 0.11 mag difference from 2013 FY27 being 0°.44 further away from true opposition in May than the March observations.

From the above March and May *r*-band observations, we find a phase coefficient of $\beta = 0.25 \pm 0.03$ mag per deg for 2013 FY27. We show in Figure 5 the phase coefficients for the largest TNOs using data from Buie et al. (1997), Sheppard & Jewitt (2002, 2003), Rabinowitz et al. (2007), Sheppard (2007), Benecchi & Sheppard (2013), Alvarez-Candal et al. (2016) and Ayala-Loera et al. (2018). We confirm the finding in Sheppard (2007) that the largest few TNOs, which are all neutral in color with high albedos, show the lowest phase coefficients (Figure 6). The lower phase coefficient is likely from back scattering off a high albedo surface. 2013 FY27 has a higher-than-typical TNO phase coefficient, which are mostly in the

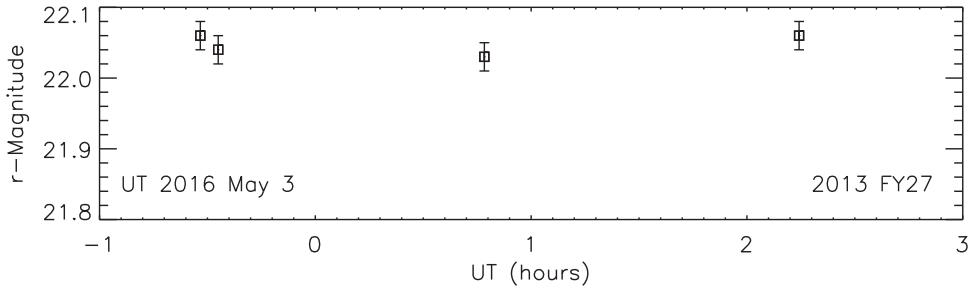

Figure 3. *r*-band photometry over a few hours for 2013 FY27 from the *Magellan* telescope on UT 2016 May 3. Again, no obvious short-term variations are seen. Combining the 2016 May observations with the 2016 March observations allows for the determination of the phase curve for 2013 FY27.

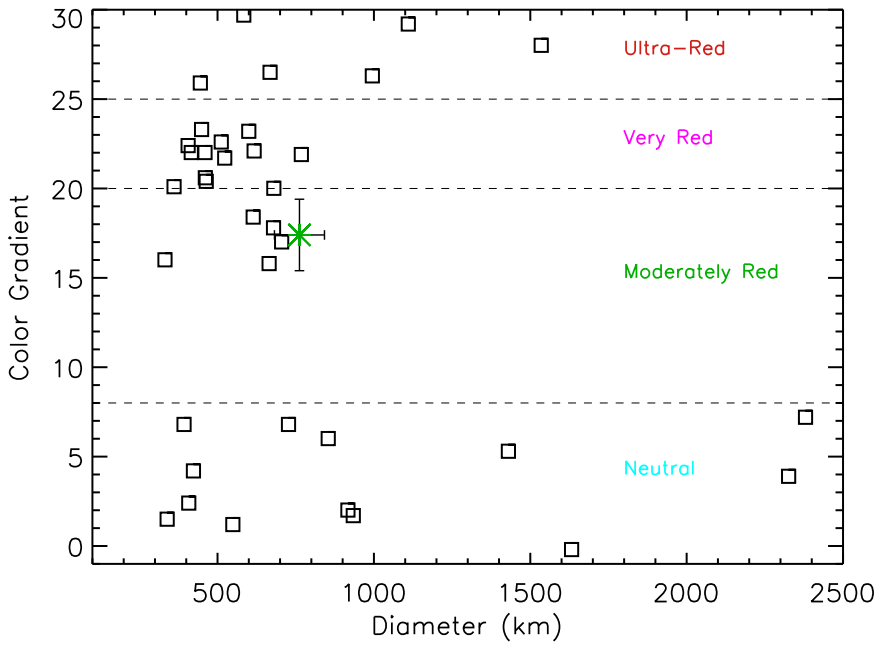

Figure 4. The colors of the largest TNOs. It is apparent that the largest 10 TNOs have either very neutral or ultra-red colors. Only objects with diameters below about 800 km start to show moderately red colors. Since neutral and ultra-red material are associated with volatiles and organics, this might suggest objects greater than 800 km have modified or resurfaced their surfaces in some way compared to smaller objects, possibly from differentiation or cryovolcanism. 2013 FY27 is one of the largest known moderately red TNOs shown by the green asterisk. Surprisingly, there are no moderately large or larger TNOs with color gradients between about 8 and 15 while the largest do not have color gradients between about 8 and 25. Error bars shown for 2013 FY27 are similar to the error bars of the other TNOs which have been removed for clarity.

0.10 to 0.20 mag per degree range. This higher phase coefficient could signify different grain properties on 2013 FY27's surface compared to the typical TNO or might be a sign of a very long and significant rotational light curve that would not be seen in a period of three days or less.

For main-belt asteroids, it appears the higher the phase coefficient, the lower the surface albedo (Belskaya & Shevchenko 2000). But main-belt asteroids likely have different compositions and usually have lower phase coefficients than the TNOs. In addition, most asteroid phase curves are based over a much larger range of phase angles, in which the TNOs are not able to be viewed as they typically stay below about 2° as seen from Earth. The opposition surge, when an object gets much brighter at very low phase angles from back-scattering effects, starts around 0.°1 to 0.°2 (Belskaya et al. 2008). The 2013 FY27 optical observations obtained at phase angles 0.17 and 0.18 degs in 2016 March may have a small contribution from the opposition surge, but are likely not strongly affected by any opposition surge as the observations are just at the start of any possible brigthness surge.

2.4. Optical Absolute Magnitude

The reduced magnitude of a solar system object is the magnitude it would have if it were observed simultaneously at a geocentric (Δ) and heliocentric (R) distance of 1 au with a phase angle of $\alpha = 0$ deg:

$$M_R(1, 1, 0) = m_R - 5\log(R\Delta) + (\alpha \times \beta). \quad (4)$$

Thus, the reduced magnitude gives you the brightness of an object independent of observing geometry. The reduced magnitude brightness is for the most part only dependent on the size and albedo of an object.

When an object is observed away from true opposition of $\alpha = 0$ deg, the reduced magnitude can be expressed as

$$M_R(1, 1, \alpha) = m_R - 5\log(R\Delta). \quad (5)$$

From Equation (5), we find the reduced magnitude of 2013 FY27 at $\alpha = 0.18$ deg is 2.90 ± 0.02 mag in the *r*-band during the 2016 March observations. For the 2016 May observations, we find the reduced magnitude is 3.01 ± 0.02 mag at $\alpha =$

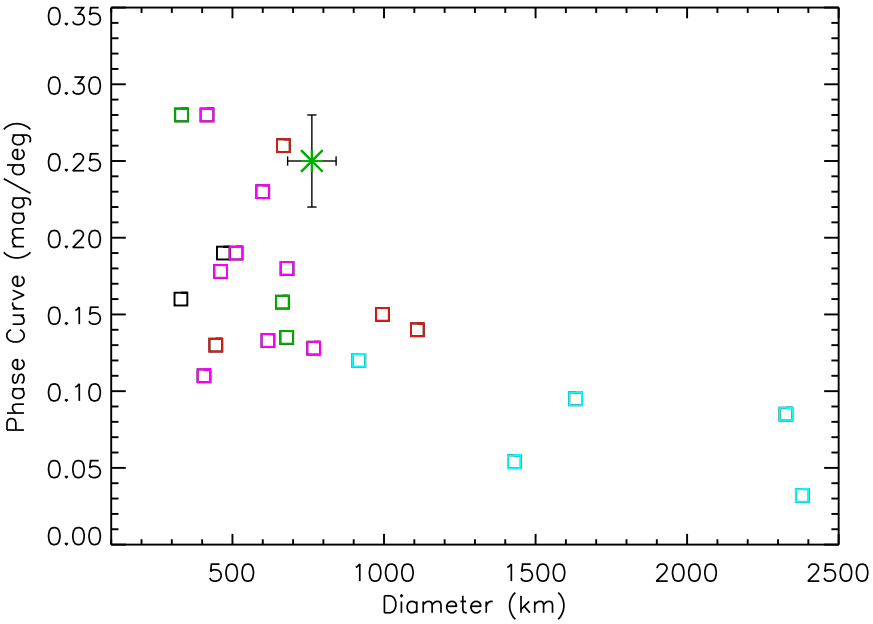

Figure 5. The phase coefficients, β, for the largest TNOs. The largest few TNOs, all with neutral colors and high albedos, have generally lower phase coefficients. Most other TNOs have phase coefficients between about 0.12 and 0.20 mag per deg. 2013 FY27 is shown by the asterisk and appears to have a higher-than-normal phase coefficient. Errors have been removed for clarity, but are generally a few hundredths of a mag per deg.

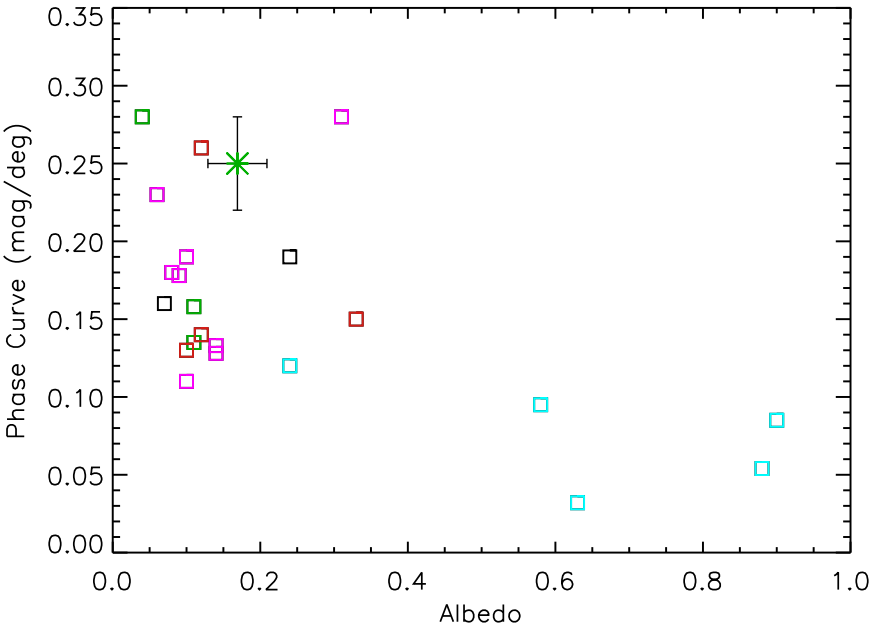

Figure 6. Same as Figure 5, but comparing albedo instead of diameter to the phase coefficient. It is clear the few very high albedo objects are all neutral in color and have the lowest phase coefficients.

0.62 deg because the object is further from opposition and thus fainter from showing a less illuminated face toward Earth.

To calculate the reduced magnitude of 2013 FY27 when at zero degrees phase angle, we use the linear phase coefficient found above of $\beta = 0.25$ mag per deg, the phase angle the observations were made at (α) and Equation (4). So 2013 FY27 should be $0.25\,\mathrm{mag\,deg^{-1}} \times 0.18\,\mathrm{deg} = 0.05$ mag brighter when at 0 deg phase angle compared to 0.18 deg phase angle assuming a linear phase function. Thus we find $M_r(1, 1, 0) = 2.85 \pm 0.02$ mag. From the transformation equations in Smith et al. (2002), we find the Johnson–Kron–Cousins R-band reduced magnitude is $M_R(1, 1, 0) = 2.59 \pm 0.02$ mag. Using the color found for 2013 FY27 of $V - R = 0.56 \pm 0.03$ mag, we find $M_V(1, 1, 0) = 3.15 \pm 0.03$ mag, which we take as the absolute magnitude H of 2013 FY27. This is slightly fainter than the current value used at the minor planet center for 2013 FY27, which is $H = 3.0$ mag. This slight difference in the absolute magnitudes is to be expected as Sheppard (2007) found the Minor Planet Center is routinely off by several tenths of magnitudes from well measured calculated values of the absolute magnitude, likely because the Minor Planet Center uses all photometry from multiple sources and filters, some of which have low signal to noise and thus large uncertainties. Though the absolute magnitude H generally uses a curved phase function as defined in Bowell et al. (1989), Sheppard (2007) found the reduced magnitude for TNOs using a linear

phase function with β is similar to within a few hundredths of the absolute magnitude phase function used in Bowell et al. (1989).

An important optical reference is to determine the optical brightness of 2013 FY27 at the time of the ALMA observations in late 2017 December and early 2018 January. The phase angle and distance of 2013 FY27 at the time of the ALMA observations is very similar to the 2016 May 3 observations from *Magellan*. Thus, we should be able to use the 2016 May 3 photometry as the base for the optical photometry during the ALMA observations. At this time $m_r = 22.04 \pm 0.02$, $m_g = 22.80 \pm 0.03$ and $m_i = 21.73 \pm 0.03$ mag, giving from color transformations using Smith et al. (2002) $m_R = 21.79 \pm 0.02$, $m_V = 22.35 \pm 0.03$ and $m_I = 21.27 \pm 0.03$ mag.

3. ALMA Observations

The Atacama Large Millimeter Array (ALMA) observations were taken on UT 2017 December 29 and 30 and 2018 January 04 in ALMA Cycle 5 under Project 2017.1.01662.S (Table 1). At that time, the array was configured with 46 antennas and a maximal distance between antennas (maximum baseline) of 2500 m. We used Band 3 in the standard continuum setup centered at 97.5 GHz, with a total encompassed bandwidth of 8 GHz. For such a cold object, Band 3 provides the best sensitivity in the continuum among all the ALMA bands making it the best to use as a first thermal detection attempt. The ALMA observations consisted of three sets of 66 minutes observations, one each on 2017 December 29 and 30 and another on 2018 January 04. The combined observations totaled of 3.3 hr of ALMA time, with 2.2 hr of that integrating on the source. The rest of the observation time was spent on quasars used as bandpass, flux, and gain calibrators.

Interferometric measurements consist in visibilities, which are complex numbers corresponding to signal cross-correlations between each pair of antennas. For each of the observations, visibilities were calibrated using the ALMA calibration pipeline in the Common Astronomy Software Applications package (CASA; McMullin et al. 2007), to correct for the spectral response and temporal gain variations of the instrument. The absolute flux scale was assessed using the well monitored quasar J1127-1857 as a reference.

The three sets of observations were then combined, spectrally averaged and stacked into one visibility set. To obtain a continuum image, inverse Fourier transform and deconvolution were applied to the combined visibilities set. Since this experiment is a point-source detection, which does not depend on spatial resolution, natural weighting was used to maximize sensitivity (at the expense of beam size), giving the final image an rms of 5.5 microJy. The synthesized beam was 0.50×0.42 arcsec in the natural-weighted image. 2013 FY27 was found very near the center of the image as expected, and was 25 microJy bright (Figure 7). This gives the ALMA detection of 2013 FY27 a signal-to-noise ratio of about 4.5. To assess the quality of the flux calibration, we compared the results given by the calibration pipeline using J1127-1857 as a reference to the expected flux value for the phase calibrator J1058+0133, which is a relatively bright and well monitored quasar. The good match between the retrieved and expected flux for J1058+0133 allows us to determine that the absolute flux calibration is accurate at the 3 to 4 percent level.

4. Size and Albedo of 2013 FY27

To first order, the thermal flux from an object is proportional to $D^2(1-p_V q)$, where D is the effective diameter, p_V is the geometric albedo in V-band, and q is the phase integral. The reflected sunlight in the V-band from the same object is proportional to $D^2 p_V$. The phase integral for TNOs can be approximated by $q = 0.336 p_V + 0.479$ (Brucker et al. 2009; Brown & Butler 2017). Thus, we have two equations that can be solved for the two unknowns of diameter and albedo (D and p_V; see e.g., Fernandez et al. 2013).

The most common method to determine the size and albedo of an object with single-epoch thermal photometry, as here with 2013 FY27, is to use the Near-Earth Asteroid Thermal Model (NEATM) of Harris (1998). Some basic assumptions used in NEATM are that (i) the object is spherical; (ii) the phase darkening of the thermal emission is entirely dependent on how much of the lit-up hemisphere of the object is facing Earth, and (iii) the basic dayside surface temperature falls off from the subsolar point as $\cos^{1/4}\theta$, where θ is the local zenith angle, and there is no thermal emission from the nightside.

These NEATM assumptions are reasonable for 2013 FY27. 2013 FY27 is probably close to spherical as it is likely large and there is little if any apparent shape-induced rotational modulation of our optical photometry (Section 2.1). Our observations were obtained at very small phase angles and thus phase-darkening uncertainties should be minimal. Regarding the temperature map, the NEATM is appropriate for a "slow rotator," i.e., an object whose thermal inertia is sufficiently low, and rotation period sufficiently long, that the object has no thermal memory. In NEATM, deviation from a zero-thermal memory situation is encapsulated in the beaming parameter, η, which will account for the different temperatures expected for an object with some thermal memory (Ferrari & Lucas 2016). A value of $\eta = 1$ corresponds to the zero-thermal memory situation, and a value of $\eta > 1$ applies to cases with thermal memory, with the higher the value, the more memory (such as the case of a quick rotator or a large thermal inertia). For our analysis of 2013 FY27, since we have measurements at only one thermal wavelength, we cannot independently determine what the beaming parameter should be. However we can use other TNO measurements to examine what would be appropriate to assume. Lellouch et al. (2013, 2017), in a study of the thermal emission from several TNOs as observed with ALMA, *Herschel*, and *Spitzer*, found that the thermal inertias of these bodies are quite low, at least an order of magnitude below that of the Moon. It is likely safe to assume that 2013 FY27 is similar, and so should be close to acting like a slow rotator in the NEATM model for reasonable values of its rotation period. Lellouch et al. (2017) advise using a value of $\eta = 1.175$ for TNOs observed with ALMA, so we adopt that value here. The other assumptions that go into NEATM are the emissivity and the visible-wavelength phase law. For the former, we assume a value of 0.70, as suggested by Lellouch et al. (2017). For the latter, we apply our results from Section 2.3, where $\beta = 0.25$ mag deg^{-1}.

The results of our application of the NEATM to the 2013 FY27 photometry are shown in Figure 8. We used a flux density from thermal emission of 25.0 ± 5.5 μJy at a wavelength of 3.075 mm, and a V-band magnitude of 22.35 ± 0.03 to fit D and p_V. The thermal emission error bar incorporates the ~4% uncertainty in the absolute calibration. Since there are zero degrees of freedom (using two

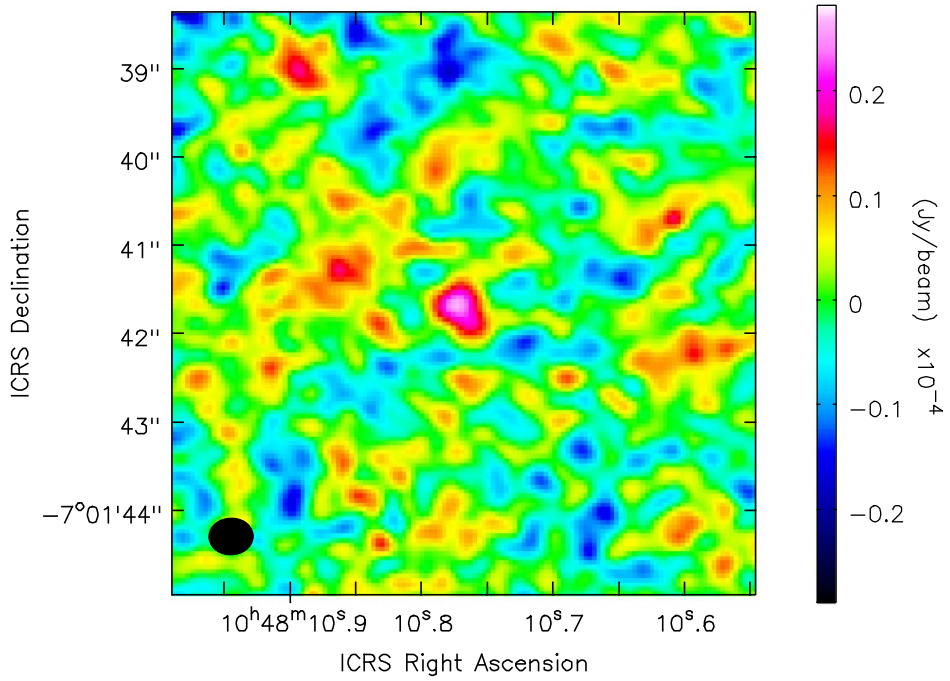

Figure 7. Stacked ALMA image showing the detection of 2013 FY27, which appeared at the center of the image as expected. The ALMA beam size 0.50 × 0.42 arcsec is shown by the black oval in the lower left.

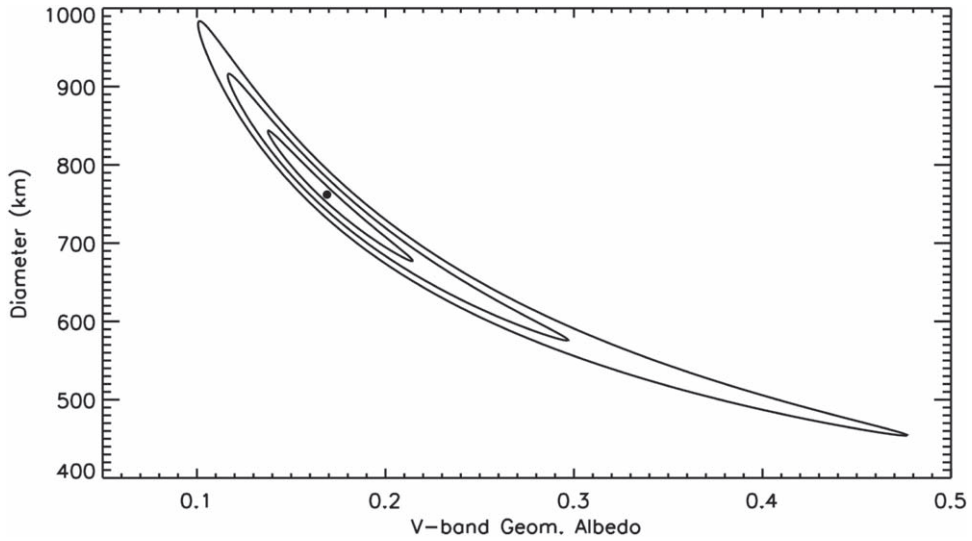

Figure 8. Contour plot showing the goodness of fit of NEATM to our millimeter and visible photometry that results in estimates of 2013 FY27's diameter and geometric albedo. The center dot is the location of the best fit, and the contours extending out from that point represent unreduced χ^2 values of 1, 2, and 3. We take a good fit to be where $\chi^2 \leqslant 1$, giving an effective area-equivalent diameter of $D = 765^{+80}_{-85}$ km and albedo of $p_V = 0.17^{+0.045}_{-0.030}$ for the 2013 FY27 system.

measurements to fit two parameters), we cannot formerly calculate a reduced-χ^2; instead, we use χ^2 itself. The contour plot in Figure 8 shows contours of $\chi^2 = 1$, 2, and 3, and we report an error bar on the best-fitting parameters to correspond to the $\chi^2 = 1$ level. We find that the best fit for 2013 FY27 is an effective area-equivalent diameter of $D = 765^{+80}_{-85}$ km and $p_V = 0.17^{+0.045}_{-0.030}$. The two error bars are correlated, as the elongated contours show. The errors on D and p_V we report here are from the uncertainty in the photometry including the absolute calibration of the standard sources in both the visible and thermal. Incorporating the potential uncertainty in the assumed parameters such as the beaming parameter and effective slow rotation period is tricky, but could add some five percent uncertainty to the calculation. As noted in Section 5 below, a satellite some three orders of magnitude fainter than 2013 FY27 was found in *HST* data. Assuming the satellite has a similar albedo as the primary, the satellite is about 186^{+25}_{-26} km in diameter, making the primary slightly smaller than calculated above at $D = 742^{+78}_{-83}$ km.

4.1. Discussion of Dwarf Planet Diameters, Albedos, and Colors

An albedo of about 17% is on the high end for a moderately red object but consistent with the other moderately red and moderately sized dwarf planet TNOs (Figure 1). 2013 FY27 is

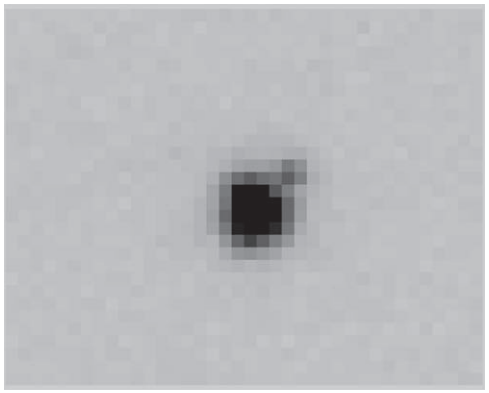

Figure 9. The discovery image of a satellite around 2013 FY27 from the *Hubble Space Telescope*. The image is in the F350LP filter with the satellite 3.0 ± 0.2 mag fainter and about 0.17 arcsec with a position angle of about 135° with respect to the primary.

one of the largest, if not the largest, moderately red TNO. All TNOs larger than 2013 FY27, of which there are about 10, have either ultra-red colors or neutral colors (see Figure 4). The TNOs with similar sizes and smaller than 2013 FY27 (diameters <800 km) start to show an abundance of moderately red or very red colors, unlike the largest 10 objects, which do not show any of these middle surface colors and only the extreme surface colors.

This suggests something is or has physically changed the surfaces of the largest 10 TNOs with diameters above 800 km compared to the TNOs with diameters smaller than 800 km. TNOs above 800 km are likely more fully differentiated than TNOs below 800 km, which we believe would make them have significantly different types of surface composition. TNOs above about 800 km could also have enough self gravity to retain certain ices such as methane more readily on their surfaces than the smaller TNOs. Neutral colored surfaces are generally associated with fresh water ice while ultra-red surfaces are associated with organics and possibly other ices such as methanol and methane (Fraser et al. 2015). The color differences may originate from the fact that TNOs above 800 km retained enough internal heat to remain active longer or even to this day, to resurface their surfaces from possible cryovolcanism type events, like possibly occurring on Pluto or Quaoar (Jewitt & Luu 2004; Neveu et al. 2015; Stern et al. 2015, 2018; Grundy et al. 2016; Bhatia & Sahijpal 2017; Desch & Neveu 2017; Bierson et al. 2018; Saxena et al. 2018). As TNOs below 800 km still show neutral and ultra-red surfaces as well as very red and moderately red surfaces, the moderately red surfaces might be a signature of a very old surface that has been bombarded by high-energy photons, particles, and micrometeorites over long periods of time, while the extreme colors are more of a sign of fresher surfaces from recent collisions or activity. Further analysis is required to determine why the largest TNOs do not show moderately red surfaces, but Figure 1 strongly suggests there is some kind of surface change around 800 km in diameter for TNOs.

5. Satellite Discovered around 2013 FY27

We observed 2013 FY27 with the *Hubble Space Telescope* (*HST*) on UT 2018 January 15 to look for possible satellites (*HST* Program GO-15248). Four 545-second images were taken with *HST* between 01:24 and 02:30 hr UT in the F350LP wide band filter (central wavelength of 5859 Angstroms) using the WFC3/UVIS instrument with a pixel scale of 0.04 arcsec per pixel (MacKenty et al. 2014). An obvious point source was detected about 0.17 arcsec at a position angle of 135 degs from the primary (Figure 9). The satellite was seen in all four images and moved along with the motion of the primary, which was about −1.47 and 0.34 arcsec an hour in R.A. and decl., respectively. This detection was reported as a satellite of 2013 FY27 to the International Astronomical Union (see CBET 4537: Sheppard 2018). No satellite motion relative to the primary was detected between the first and last (fourth) image from *HST*, confirming its association with the primary and likely ruling out an extremely fast orbital period of a few days or less around the primary. The four *HST* images were aligned with respect to the primary and coadded to search for additional fainter satellites, but nothing obvious was detected to about 27.5 mag within a tenth to tens of arcseconds of the primary.

At the time of the *HST* observations, 2013 FY27 was 79.48 au from the Earth. Thus a 0.17 arcsec separation means the satellite was at least 9800 km from the primary. The newly discovered satellite was 3.0 ± 0.2 mag fainter than the primary in the optical. Thus, the diameter of the satellite, if assuming the same albedo as the primary, would be about 3.9 times smaller than the primary or about 186 km in diameter.

Additional *HST* observations of 2013 FY27 and its satellite have been obtained in 2018 May and July under *HST* Program 15460. A full analysis of the new *HST* data will allow for the determination of the satellite orbit, and with the albedo reported in this work, a bulk density of the system can be determined giving insight into the composition and structure. The full detailed analysis using all of the *HST* observations for 2013 FY27 will be part of a future paper on the satellite and its orbit around 2013 FY27. We note that in Figure 7, there appears to be an extension of the ALMA signal to the southwest of the primary. This is unlikely to be the satellite of 2013 FY27 as we believe the satellite is nearly edge-on, and thus should only show up to the southeast and northwest of the primary. Obtaining the full orbit of the satellite will allow us to predict where it should have been during the ALMA observations and further analysis of the ALMA data and 2013 FY27's satellite is left for the next paper on the full orbit of the 2013 FY27 system.

5.1. Discussion of Dwarf Planet Satellites

All of the largest known TNOs, those with diameters well over 1000 km, irrespective of their dynamical class, have known satellites (Pluto, Eris, Makemake, 2007 OR10, Haumea, and Quaoar) and now 11 of the top 15 largest TNOs have known satellites (Figure 10). All of the satellites of these largest objects are significantly smaller than the primary and have relatively close orbits that are indicative of collisional formation or rotational fission (Brown et al. 2006; Noll et al. 2008; Ortiz et al. 2012b; Parker et al. 2016; Kiss et al. 2017; Brown & Butler 2018). It is remarkable that satellites seem to be the norm and not the exception for the largest objects. This appears to suggest the collisional formation of Earth's moon and the satellites of Mars are normal outcomes of the planet formation process (Mercury and Venus likely have no satellites simply because their closeness to the massive Sun makes tidal interactions too strong for most satellite orbits around these planets to be stable over the age of the solar system).

Though we do not know the full orbit of the satellite for 2013 FY27, its small size relative to the primary and relatively

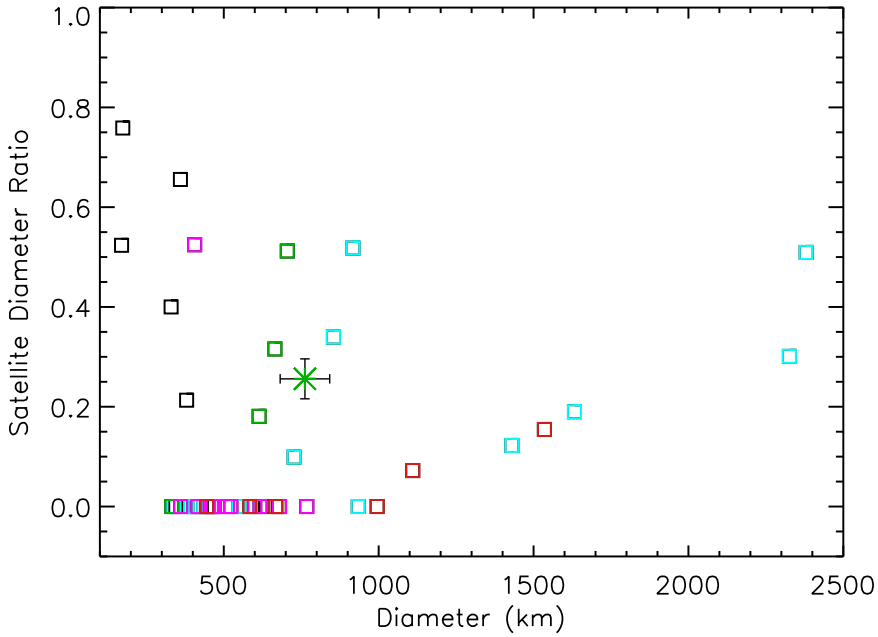

Figure 10. The largest known TNOs and their satellite's diameter to primary diameter ratio. TNOs with a zero size ratio do not have a known satellite. For Pluto and Haumea, which have multiple known satellites, the largest known satellite was used to determine the satellite-to-primary diameter ratio. There appears to be a break around 900 km where the satellite-to-primary diameter ratio becomes much smaller for the largest TNOs, with only Pluto being above 0.3.

close distance suggest the satellite was likely created by a direct impact, similar to the scenarios envisioned for the other known satellites of the dwarf planets (Canup 2011; McKinnon et al. 2017). This formation scenario is quite different than the equal-sized, distant binaries found mostly in the main Kuiper Belt, which likely did not form through direct collisions onto the primary (Schlichting & Re'em 2008; Nesvorny et al. 2010; Parker et al. 2011; Sheppard et al. 2012).

Barr & Schwamb (2016) suggest that there are two possible collisional formation scenarios that could create the close-in satellites found around all the largest TNOs. High-energy direct collisions could remove the ice from the primary, leaving a dense primary and small ice rich satellite. A glancing indirect collision would leave the primary volatile rich and thus of low density and could create larger satellites of similar composition to the primary. 2013 FY27 can be a further test to this theory through determining its density from knowing the full orbit of the satellite around the primary as well as looking at the surfaces of the primary and secondary for similarities or differences. We note in Figure 10 there appears to be a break in the ratio of the satellite size to the primary size for TNOs larger than about 900 km. TNOs larger than about 900 km have relatively small satellites compared to the primary (though Pluto somewhat breaks this trend). Many of the smaller TNOs appear to have satellites that are relatively large compared to the primary, with some approaching equal-sized binaries starting around 400 km in diameter.

6. Summary

2013 FY27 is intrinsically the brightest TNO not yet observed for its basic physical properties. 2013 FY27's absolute magnitude of nearly 3 mag means it likely has a size that is near the transition region between the largest few TNOs (which show high albedos and high densities) and the smaller TNOs (which show low to moderate albedos and densities). We observed 2013 FY27 over optical and thermal wavelengths at several telescopes to determine its physical characteristics for the first time and compared it to the other dwarf planets.

(1) The geometric albedo of 2013 FY27 was found to be $p_V = 0.17^{+0.045}_{-0.030}$. The effective area-equivalent diameter of the 2013 FY27 system is $D = 765^{+80}_{-85}$ km. Assuming the newly discovered satellite around 2013 FY27 has a similar albedo as the primary, the satellite is about 186^{+25}_{-26} km in diameter, making the primary slightly smaller than the effective area-equivalent diameter of the system at $D = 742^{+78}_{-83}$ km.

(2) The color of 2013 FY27 was found to be moderately red with a spectral gradient of $S = 17 \pm 2$. This makes 2013 FY27 one of the largest known moderately red TNOs. All TNOs larger than about 800 km in size, of which there are about 10 known, only show neutral or ultra-red surface colors. This could be because the largest several TNOs have different or fresher surfaces than TNOs smaller than 800 km from possible cryovolcanism, differentiation, and/or abundant exposed surface ices. The TNOs only start to show moderately red colors for objects less than about 800 km in diameter, and they appear to be very abundant below this threshold. As there is also neutral and ultra-red TNOs below 800 km, it suggests the moderately red color might be an indication of an old surface while the more neutral and ultra-red colors in the smaller TNOs could be fresh surfaces exposed from recent impacts or other processes.

(3) A satellite of 2013 FY27 was found in *Hubble Space Telescope* observations of 2013 FY27. It is some 3.0 ± 0.2 mag fainter and was 0.17 arcsec away from the primary at discovery. The satellite diameter to primary diameter ratio is a little larger than most of the ratios found for the largest TNOs. There appears to be a difference in the satellite-to-primary size ratios starting around the TNOs over about 900 km. For TNOs with primaries less than 900 km, the satellite-to-size ratio increases as the primary size decreases until around 400 km, when one starts to approach equal-sized binaries. For TNOs larger than 900 km, the satellite-to-primary size ratio is generally smaller, with Pluto being an exception.

(4) 2013 FY27 was monitored over minutes, hours, and days with no obvious short-term variability detected in the *r*-band. The most likely reason for no measurable short-term light curve is that 2013 FY27 is nearly spherical in shape with no significant albedo variations on its surface to allow for a measurable rotational period. 2013 FY27 was further monitored in the *r*-band over months to find its linear phase coefficient of $\beta = 0.25 \pm 0.03$ mag deg^{-1}. This is a slightly higher-than-normal TNO phase coefficient, but reasonable for a moderate albedo surface, unlike the lower phase coefficients found for very high albedo TNO surfaces. The reduced magnitude of 2013 FY27 was found to be $M_r(1, 1, 0) = 2.85 \pm 0.02$ and $M_V(1, 1, 0) = 3.15 \pm 0.03$ mag.

We thank D. Ragozzine for comments on the manuscript and sharing the initial analysis of the 2013 FY27 satellite orbit. This paper makes use of the following ALMA data: ADS/JAO. ALMA#2017.1.01662.S. ALMA is a partnership of ESO (representing its member states), NSF (USA) and NINS (Japan), together with NRC (Canada), NSC and ASIAA (Taiwan), and KASI (Republic of Korea), in cooperation with the Republic of Chile. The Joint ALMA Observatory is operated by ESO, AUI/NRAO and NAOJ. The National Radio Astronomy Observatory is a facility of the National Science Foundation operated under cooperative agreement by Associated Universities, Inc. This work is based in part on NASA/ESA *Hubble Space Telescope* Cycle 25 Program 15248 observations. This paper includes data gathered with the 6.5 m *Magellan* Telescopes located at Las Campanas Observatory, Chile.

ORCID iDs

Scott S. Sheppard https://orcid.org/0000-0003-3145-8682
Yanga R. Fernandez https://orcid.org/0000-0003-1156-9721
Arielle Moullet https://orcid.org/0000-0002-9820-1032

References

Alvarez-Candal, A., Ortiz, J., Morales, N., et al. 2014, A&A, 571, 48
Alvarez-Candal, A., Pinilla-Alonso, N., Ortiz, J., et al. 2016, A&A, 586, 155
Ayala-Loera, C., Alvarez-Candal, A., Ortiz, J., et al. 2018, MNRAS, 481, 1848
Barr, A., & Schwamb, M. 2016, MNRAS, 460, 1542
Barucci, M., Belskaya, I., Fulchignoni, M., & Birlan, M. 2005, AJ, 130, 1291
Barucci, M., Morea Dalle Ore, C., Alvarez-Candal, A., et al. 2010, AJ, 140, 2095
Basri, G., & Brown, M. 2006, AREPS, 34, 193
Belskaya, I., Levasseur-Regourd, A., Shkuratov, Y., & Muinonen, K. 2008, in The Solar System Beyond Neptune, ed. M. Barucci et al. (Tucson, AZ: Univ. Arizona Press), 115
Belskaya, I., & Shevchenko, V. 2000, Icar, 147, 94
Benecchi, S., & Sheppard, S. 2013, AJ, 145, 124
Benedetti-Rossi, G., Sicardy, B., Buie, M., et al. 2016, AJ, 152, 156
Bhatia, G., & Sahijpal, S. 2017, M&PS, 52, 2470
Bierson, C., Nimmo, F., & McKinnon, W. 2018, Icar, 309, 207
Bowell, E., Hapke, B., Domingue, D., et al. 1989, Asteroids II (Tucson, AZ: Univ. Arizona Press), 524
Braga-Ribas, F., Sicardy, B., Ortiz, J., et al. 2013, ApJ, 773, 26
Brown, M. 2013, ApJL, 778, L34
Brown, M., & Butler, B. 2017, AJ, 154, 19
Brown, M., & Butler, B. 2018, AJ, 156, 164
Brown, M., Ragozzine, D., Stansberry, J., & Fraser, W. 2010, AJ, 139, 2700
Brown, M., Schaller, E., & Fraser, W. 2012, AJ, 143, 146
Brown, M., van Dam, M., Bouchez, A., et al. 2006, ApJ, 639, 43
Brucker, M., Grundy, W., Stansberry, J., et al. 2009, Icar, 201, 284
Buie, M., Tholen, D., & Wasserman, L. 1997, Icar, 125, 233
Canup, R. 2011, ApJ, 141, 35
Chin, C., Chen, S., Liu, M., Huang, T., & Wu, Y. 2016, ApJS, 224, 17
Dalle Ore, C., Barucci, M., Emery, J., et al. 2015, Icar, 252, 311
Desch, S., & Neveu, M. 2017, Icar, 287, 175
Dias-Oliveira, A., Sicardy, B., Ortiz, J., et al. 2017, AJ, 154, 22
Doressoundiram, A., Boehnhardt, H., Tegler, S., & Trujillo, C. 2008, in The Solar System Beyond Neptune, ed. M. Barucci et al. (Tucson, AZ: Univ. Arizona Press), 91
Elliot, J., Person, M., Zuluaga, C., et al. 2010, Natur, 465, 897
Fernandez, Y., Kelley, M., Lamy, P., et al. 2013, Icar, 226, 1138
Ferrari, C., & Lucas, A. 2016, A&A, 588, 133
Fornasier, S., Lellouch, E., Muller, T., et al. 2013, A&A, 555, 15
Fraser, W., Brown, M., & Glass, F. 2015, ApJ, 804, 31
Gerdes, D., Sako, M., Hamilton, S., et al. 2017, ApJL, 839, L15
Grundy, W. 2009, Icar, 199, 560
Grundy, W., Binzel, R., Buratti, B., et al. 2016, Sci, 351, 9189
Grundy, W., Porter, S., Benecchi, S., et al. 2015, Icar, 257, 130
Hainaut, O., Boehnhardt, H., & Protopapa, S. 2012, A&A, 546, 115
Harris, A. 1998, Icar, 131, 291
Jewitt, D. 2002, AJ, 123, 1039
Jewitt, D., & Luu, J. 2004, Natur, 432, 731
Kiss, C., Marton, G., Farkas-Takacs, A., et al. 2017, ApJ, 838, 1
Kovalenko, I., Doressoundiram, A., Lellouch, E., et al. 2017, A&A, 608, 19
Lacerda, P., Fornasier, S., Lellouch, E., et al. 2014, ApJL, 793, L2
Lantz, C., Brunetto, R., Barucci, M., et al. 2017, Icar, 285, 43
Lebofski, L. A., Sykes, M. V., Tedesco, E. F., et al. 1986, Icar, 68, 239
Lellouch, E., Kiss, C., Santos-Sanz, P., et al. 2010, A&A, 518, 147
Lellouch, E., Moreno, R., Muller, T., et al. 2017, A&A, 608, 45
Lellouch, E., Santos-Sanz, P., Lacerda, P., et al. 2013, A&A, 557, A60
Lim, T., Stansberry, J., Muller, T., et al. 2010, A&A, 518, 148
Lo, J., Chou, S., Peng, Y., Lin, M., Lu, H., & Cheng, B. 2015, ApJS, 221, 20
Luu, J., & Jewitt, D. 1996, AJ, 112, 2310
MacKenty, J., Baggett, S., Brammer, G., et al. 2014, Proc. SPIE, 9143, 914328
McKinnon, W., Stern, S., Weaver, H., et al. 2017, Icar, 287, 2
McMullin, J. P., Waters, B., Schiebel, D., Young, W., & Golap, K. 2007, in ASP Conf. Ser. 376, Astronomical Data Analysis Software and Systems XVI, ed. R. A. Shaw, F. Hill, & D. J. Bell (San Francisco, CA: ASP), 127
Moroz, L., Baratta, G., Strazzulla, G., et al. 2004, Icar, 170, 214
Muller, T., Lellouch, E., Stansberry, J., et al. 2010, A&A, 518, 146
Nesvorny, D., Youdin, A., & Richardson, D. 2010, AJ, 140, 785
Neveu, M., Desch, S., Shock, E., & Glein, C. 2015, Icar, 246, 48
Noll, K., Grundy, W., Chiang, E., Margot, J., & Kern, S. 2008, in The Solar System Beyond Neptune, ed. M. Barucci et al. (Tucson, AZ: Univ. Arizona Press), 345
Ortiz, J., Santos-Sanz, P., Sicardy, B., et al. 2017, Natur, 550, 219
Ortiz, J., Sicardy, B., Braga-Ribas, F., et al. 2012a, Natur, 491, 566
Ortiz, J., Thirouin, A., Campo Bagatin, A., et al. 2012b, MNRAS, 419, 2315
Pal, A., Kiss, C., Muller, T., et al. 2012, A&A, 541, 6
Parker, A., Buie, M., Grundy, W., & Noll, K. 2016, ApJ, 825, 9
Parker, A., Kavelaars, J., Petit, J., et al. 2011, ApJ, 743, 1
Perna, D., Barucci, M., Fornasier, S., et al. 2010, A&A, 510, 53
Rabinowitz, D., Schaefer, B., & Tourtellotte, S. 2007, AJ, 133, 26
Rambaux, N., Baguet, D., Chambat, F., & Castillo-Rogez, J. 2017, ApJ, 850, 9
Santos-Sanz, P., Lellouch, E., Fornasier, S., et al. 2012, A&A, 541, 92
Santos-Sanz, P., Lellouch, E., Groussin, O., et al. 2017, A&A, 604, 95
Saxena, P., Renaud, J., Henning, W., Jutzi, M., & Hurford, T. 2018, Icar, 302, 245
Schlichting, H., & Re'em, S. 2008, ApJ, 673, 1218
Sheppard, S. 2007, AJ, 134, 787
Sheppard, S. 2010, AJ, 139, 1394
Sheppard, S. 2012, AJ, 144, 169
Sheppard, S. 2018, CBET, 4537, 1, http://www.cbat.eps.harvard.edu/cbet/RecentCBETs.html
Sheppard, S., & Jewitt, D. 2002, AJ, 124, 1757
Sheppard, S., & Jewitt, D. 2003, EM&P, 92, 207
Sheppard, S., Lacerda, P., & Ortiz, J. 2008, in The Solar System Beyond Neptune, ed. M. Barucci et al. (Tucson, AZ: Univ. Arizona Press), 129
Sheppard, S., Ragozzine, D., & Trujillo, C. 2012, AJ, 143, 58
Sheppard, S., & Trujillo, C. 2016, AJ, 152, 221
Smith, J., Tucker, D., Kent, S., et al. 2002, AJ, 123, 2121
Stansberry, J., Grundy, W., Brown, M., et al. 2008, in The Solar System Beyond Neptune, ed. M. Barucci et al. (Tucson, AZ: Univ. Arizona Press), 161
Stellingwerf, R. 1978, ApJ, 224, 953
Stern, S., Bagenal, F., Ennico, K., et al. 2015, Sci, 350, 1815
Stern, S., Grundy, W., McKinnon, W., Weaver, H., & Young, L. 2018, ARR&A, 56, 357
Tegler, S., Cornelison, D., Grundy, W., et al. 2010, ApJ, 725, 1296
Tegler, S., Romanishin, W., & Consolmagno, G. 2016, AJ, 152, 210